photonics

MDPI

Article

Comparative Performance Analysis of Femtosecond-Laser-Written Diode-Pumped Pr:LiLuF$_4$ Visible Waveguide Lasers

Davide Baiocco [1,*], Ignacio Lopez-Quintas [2], Javier R. Vázquez de Aldana [2], Mauro Tonelli [1] and Alessandro Tredicucci [1]

[1] Dipartimento di Fisica, Università di Pisa, Largo Bruno Pontecorvo 3, 56127 Pisa, Italy
[2] Grupo de Investigación en Aplicaciones del Láser y Fotónica, Universidad de Salamanca, Pl. La Merced SN, 37008 Salamanca, Spain
* Correspondence: davide.baiocco@phd.unipi.it

Abstract: In this work, we present the operation of a femtosecond-laser-written diode-pumped visible waveguide laser based on praseodymium-doped lithium lutetium fluoride. The refractive index modification induced by the femtosecond laser in the crystal exhibits an anisotropic behavior, thus enabling the fabrication of different types of waveguides from single-track structures to stress-induced waveguides and depressed cladding structures. All the waveguides were characterized by realizing transmission measurements and the waveguide design was optimized to obtain extremely low propagation losses, equal to 0.12 dB/cm. Lasing has been achieved at 604 nm and 721 nm from different waveguides. In addition, stable continuous-wave lasing at 698 nm has been obtained in a depressed cladding waveguide. This wavelength corresponds to the one needed for the transition of the atomic clock based on the neutral strontium atom. In the end, we report the observation of laser emission at 645 nm from a depressed cladding waveguide.

Keywords: visible laser; waveguide laser; diode-pumping; femtosecond-laser writing; praseodymium

Citation: Baiocco, D.; Lopez-Quintas, I.; R. Vázquez de Aldana, J.; Tonelli, M.; Tredicucci, A. Comparative Performance Analysis of Femtosecond-Laser-Written Diode-Pumped Pr:LiLuF$_4$ Visible Waveguide Lasers. *Photonics* **2023**, *10*, 377. https://doi.org/10.3390/photonics10040377

Received: 20 February 2023
Revised: 17 March 2023
Accepted: 27 March 2023
Published: 29 March 2023

1. Introduction

The ongoing quest for compact coherent sources has led to the development of several different laser technologies. Solid state lasers (SSLs), despite the necessity of optical pumping, have the advantage of a quasi-diffraction limited beam and operate in spectral regions not covered by laser diodes. Moreover, the laser emission of SSLs possesses a narrower bandwidth compared to the one of laser diodes, corresponding to a greater frequency stability, a crucial property for metrological applications. In addition, SSLs do not suffer from aging effects shown by lased diodes [1]. A significant boost to the development of SSLs came from the invention and availability of watt-level InGaN-based laser diodes, which emit in the blue range of the visible spectrum, providing a compact and inexpensive solution for optical pumping of SSLs [2].

The ionized praseodymium can be pumped with InGaN-based laser diodes, since it shows strong absorption lines at about 445 nm, while its emission spectrum runs over all the visible range, from cyan, 480 nm, to deep red at 720 nm, containing all the lines necessary for the operation of the atomic clock based on neutral strontium atom [3–6]. Between all the materials tested as a host for praseodymium ions, the best results were obtained with fluoride single crystals because of the lower phonon energy of these crystals, the lower crystal field strength and a greater energy gap between valence and conduction band [2].

Recently, in search of more compact SSLs, guiding structures were fabricated in dielectric materials in order to obtain better overlap between the pump beam and the laser mode for all the length of the active medium. This could reflect in greater efficiencies and lower laser threshold. In 1996, Davis et al. demonstrated that it is possible to inscribe

waveguides in a transparent dielectric by irradiating it with an ultrashort laser pulse [7], causing a variation of the refractive index in the irradiated area. Since then, waveguide SSLs were developed, in particular operating in the 1–2 µm spectral range, exploiting the emission lines of neodymium [8–10], thulium [11,12] or ytterbium [13], to only report a few works. For the visible range, a few praseodymium-based waveguide lasers were obtained [14–19], due to the necessity of a low-loss waveguide in the visible range and a material with high optical quality and all the features previously described.

In this work, we present a comparative performance analysis on waveguide lasers based on praseodymium doped lithium lutetium fluoride ($LiLuF_4$, LLF), obtaining laser emissions from waveguides of different design at four distinct wavelengths: 604 nm, 645 nm, 698 nm and 721 nm. This is also the first demonstration of a praseodymium-based waveguide laser operating at 645 nm.

2. Materials and Methods

LLF is a crystal isomorph to $LiYF_4$ (YLF), being a tetragonal crystal with the structure of the scheelite ($CaWO_4$). Its lattice constants are $a = 5.124$ Å and $c = 10.54$ Å [20]. It was preferred over YLF due to its better thermomechanical properties [21]. In this host, praseodymium absorption transition $^3H_4 \rightarrow ^3P_2$ is located at 444 nm and its absorption cross section is about 1.0×10^{-19} cm^2, allowing efficient diode-based optical pumping [2]. Its fluorescence spectrum in the 600–750 nm is composed by four main transitions. The one with the greater emission cross section is the $^3P_0 \rightarrow ^3F_2$, corresponding to an emission wavelength of 640 nm in σ polarization (E//a). At the same wavelength, two peaks of low intensity (639 nm and 645 nm) are present for π polarization (E//c). For π polarization, three other peaks are present: $^3P_0 \rightarrow ^3H_6$ (604 nm), $^3P_0 \rightarrow ^3F_3$ (698 nm), $^3P_0 \rightarrow ^3F_4$ (721 nm). For sigma polarization, a strong emission is present at 607 nm ($^3P_0 \rightarrow {}^3H_6$) and minor peaks are present in correspondence of the other transitions listed before. Polarized absorption and fluorescence spectra are reported in Figure 1.

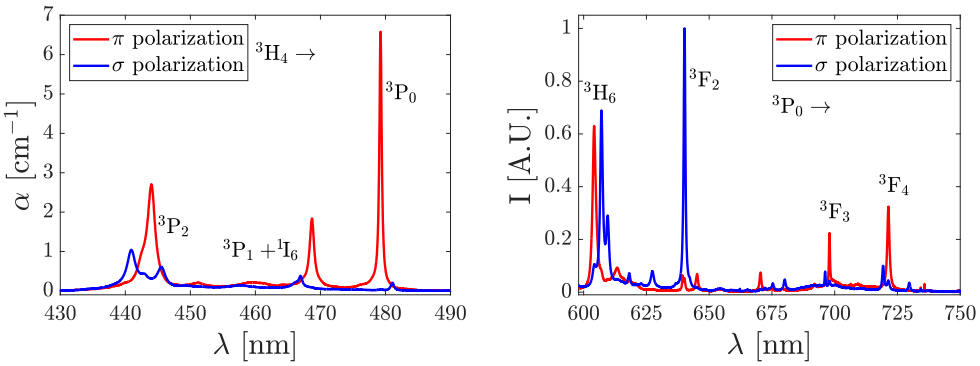

Figure 1. Polarized absorption (**left**) and fluorescence (**right**) spectra of Pr:LLF. The fluorescence spectrum for all the visible range is reported in [3]. The spectral bandwidth of the light employed for absorption measurements was 0.09 nm while the resolution of the fluorescence spectra is 0.13 nm.

High quality LLF:Pr single crystals have been grown from high purity powders (LiF, LuF_3 and PrF_3 powders from AC materials, Tarpon Springs, FL, USA), by a Czochralski furnace at the University of Pisa. The dopant concentration in the melt was of 1%. Using X-ray diffraction [3], the crystallographic axes have been identified and the boule oriented. Subsequently, two oriented samples have been carved from the boule. A known effect in growing Pr:LLF is dopant segregation [3]. This reflects in lower concentrations of Pr^{3+} ions in the grown material with respect to the nominal doping in the melt. The real dopant concentration has been estimated from absorption measurements, realized with a CARY 5000 spectrophotometer, by knowing the absorption cross section [2]. The Pr^{3+} concentration results equal to 0.2% for both samples. This value is in agreement with the one obtained by ICP analysis in [3]. Samples have been polished to obtain laser quality

facets. The final dimensions of the samples are 4 mm(a) × 4 mm(c) × 8 mm(a) for sample 1 and 4 mm(a) × 4 mm(c) × 9 mm(a) for sample 2. The waveguides were written parallel to an a-axis in both samples, resulting in a 8 mm long waveguide for sample 1 and 9 mm long for sample 2.

2.1. Waveguide Fabrication

The waveguides were fabricated in the Pr:LLF samples by using an amplified femtosecond laser system (Spitfire ACE, Spectra Physics, Milpitas, USA) that delivered 60 fs pulses with a central wavelength of 800 nm, at a repetition rate of 5 kHz. The beam profile has a nearly Gaussian shape with $M^2 < 1.2$ and it is linearly polarized perpendicularly to the scanning direction. The pulse energy was finely tuned by using a set of half-wave plate and linear polarizer, and a calibrated neutral density filter. Then, the beam was focused through a 40X microscope objective (0.65 NA) inside the crystal to produce localized damage tracks by non-linear (multiphoton) absorption. To inscribe each of the designed waveguides, the sample was moved at constant velocity with a motorized XYZ micropositioning stage (HPL-170, PiMicos, PImiCos GmbH, Karlsruhe, Germany).

In crystalline materials, the fabrication of optical waveguides by femtosecond laser irradiation is not as easy as in glasses [7] because, in many cases, it is not possible to produce a refractive index increase, able to directly confine and guide light along a certain trajectory. On the contrary, the most typical situation is that the refractive index of the crystal is decreased by the effect of the high intensity of the laser, but even in those cases it can be used anyway to design efficient waveguides [22].

In our study, we designed and fabricated waveguides with different configurations and geometries in the search for the best performance, helping us to understand the confinement mechanisms in Pr:LLF. The following waveguide types were tested:

- Circular cladding (CC): this waveguide type consists of a cladding with a reduced refractive index that is produced by multiple parallel laser damage tracks following the desired circular geometry [8]. The scanning velocity was varied between 600 µm/s and 1200 µm/s, the pulse energy between 70 nJ and 100 nJ and the separation between adjacent tracks was set to 2 µm. With these parameters CCs were inscribed with different radius.
- Circular cladding "with ears" (CC-E): in certain circumstances, propagation loss of CC waveguides is reduced by designing a more complex structure of damage tracks at the side of the claddings ("ears") that may minimize leakage from the waveguide [10]. Same parameters as CC were tested for CC-E waveguide fabrication.
- Hexagonal cladding (HC): cladding waveguides with a hexagonal geometry [23]. The separation between tracks of the cladding was set to 7 µm, and the pulse energy and scanning velocity were varied as for CC waveguides.
- Stress-induced double-line (DL): stress-induced waveguides make use of the compressive stress created at the side of the damage tracks to produce a region with increased refractive index [24]. Our design consisted of two parallel tracks with a separation of 3 µm, and two other identical tracks with a separation of 14, 16 or 20 µm. The pulse energy was varied between 90–120 nJ and the scanning velocity was set to 100 µm/s.
- Stress-induced double-line with rhombic cladding (DL-RC): same structure as DL but adding some tracks above or below the waveguide region to improve confinement [14]. DL tracks were fabricated with the same parameters as DLs and the cladding tracks with a pulse energy of 100 nJ and a scanning velocity of 100 or 500 µm/s.
- Single line (SL): it consists of a single laser scan that acts as waveguide in the cases where a refractive index increase could be produced at the damage track [24]. We have tested these structures in Pr:LLF with pulse energies between 50 and 100 nJ, and scanning velocities between 150 and 500 µm/s.

As an example, images of the cross-sections of some waveguides are shown in Figure 2.

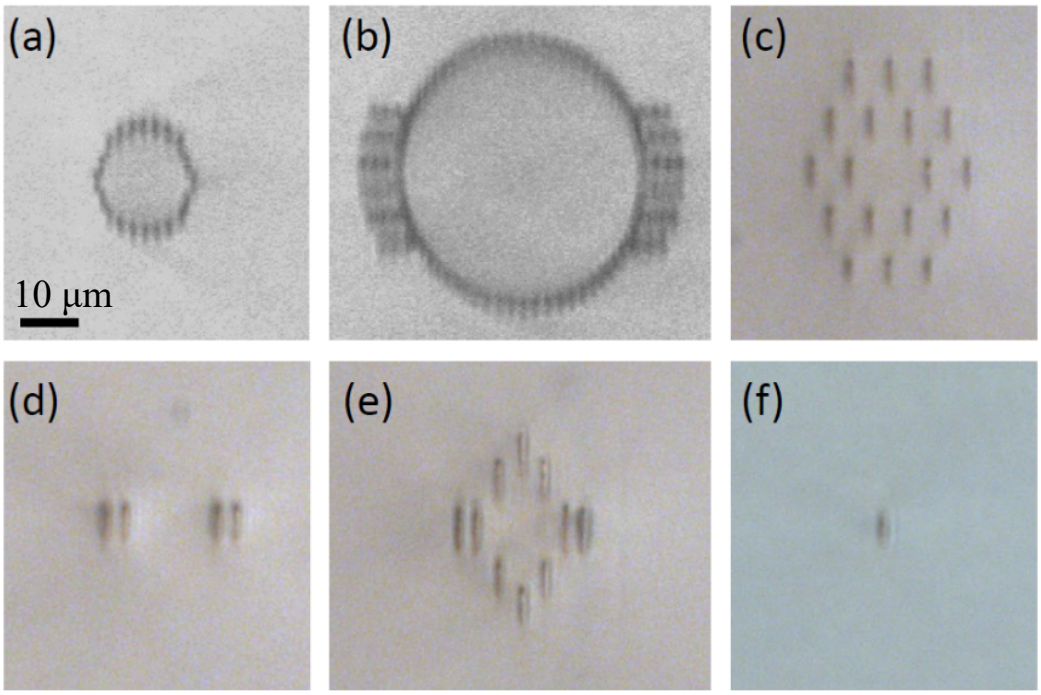

Figure 2. Optical microscope pictures of the different waveguide types fabricated in Pr:LLF, taken in transmission mode with white light illumination. The scale bar corresponds to 10 µm and it is common to all figures. (**a**) Circular cladding (CC), (**b**) circular cladding "with ears" (CC-E), (**c**) hexagonal cladding (HC), (**d**) stress-induced double-line (DL), (**e**) stress-induced double-line with rhombic cladding (DL-RC) and (**f**) single line (SL).

2.2. Waveguide Analysis

To characterize the waveguides, we initially performed coupling and transmission measurements at 632.8 nm, employing an unpolarized He-Ne laser as the source and a Glan–Thompson polarizer to control the polarization of the incident beam. The measurements were carried out both for σ-polarization and for π-polarization due to the birefringence of the host material, which could lead to a different behavior of the waveguides for different polarizations. The laser beam was focused with several lenses, obtaining the best performance with an achromatic lens of 30 mm focal length. The corresponding beam diameter at the waist was $2w_0 = 12$ µm. The light exiting from the waveguide has been collected with an OLYMPUS PLN20× microscope objective (N.A. of 0.4, manufactured by Olympus Corporation, Japan), forming an image of the confined mode on a beam profiler (BP, DataRay WinCamD-UCD15, DataRay Inc., USA). For all those measurements, the sample was placed in a custom made copper holder, which allows active temperature stabilization of the sample through a thermoelectric cooler. The whole system was placed on a 3-axes goniometer as well as a translation stage to optimize the beam coupling. The positions of both coupling and collection optics have been controlled by placing each of them on a 3D precision translation stage (THORLABS MBT616D/M, manufactured by Thorlabs Inc.). Some of the measured intensity profiles with the corresponding microscope images of the waveguide cross-sections are shown in Figure 3. Measuring the transmission efficiency of the waveguide, an upper limit for the propagation losses can be set, subtracting the effect of Fresnel losses and assuming the complete coupling of the laser beam in the waveguide. The best results for each type of waveguide are shown in Tables 1 and 2. There, the presence of confined modes, their characteristics and the upper limit on the propagation losses are reported. In the tables, the writing parameters for each waveguide are also listed. The complete data of waveguide parameters are included in Appendix B.

Some of the SL waveguides written on sample 2 (WG15-WG16 of c-cut facet and WG15, WG17-WG20 of a-cut facet) showed confinement only for σ polarization while none of the

SL waveguides confine π polarization. For DL waveguides (WG15-WG20 of sample 1), no confinement has been observed for both polarizations. Better results have been achieved from DL-RC waveguides, which confine π polarization in the core. No confinement of the σ polarization has been observed in these waveguides. A different behavior has been observed in depressed cladding waveguides, where π polarization is confined in the core and σ in the cladding. This behavior can be explained in terms of a refractive index increase at the damage tracks for σ polarization, opposed to the refractive index decrease observed for π polarization. It means that the modification produced by the femtosecond laser irradiation is highly anysotropic, as it has been reported for other crystalline material such as $LiTaO_3$ [25]. In this case, the multiple tracks that compose the waveguide act as a set of parallel waveguides (see Figure 3c), coupling a total power comparable or greater than the one confined in the core, but with a modal profile that resembles the cladding shape, which is not useful for the construction of a laser device. The waveguide design which demonstrates the lower propagation losses is the CC-E design. Except for WG10 of sample 1, those waveguides possess propagation losses lower than 0.4 dB/cm for π-polarization, a value lower than those previously reported for femtosecond-laser-written waveguides on fluorides [14,15]. In particular, waveguide WG8 of sample 1 shows an upper limit for the propagation losses of 0.12 dB/cm, a value comparable to the one observed for ultra-large area waveguides realized by helical inscription technique [16].

Table 1. Writing parameters, type of guided modes, and upper limit for the propagation losses for sample 1. WG is the waveguide number, E is the pulse energy on the sample, V is the scan velocity and T is the track separation. SM means single mode waveguide, MM stands for multimodal waveguide, CL is for a mode confined in the cladding and not in the core while - denotes a non-confined polarization. The upper limit for the losses is reported only when the radiation is confined in the core of the waveguide.

WG	Description	E [nJ]	V [µm/s]	T [µm]	Modes		α [dB/cm]	
					π	σ	π	σ
1	CC 8 µm rad.	70	600	2	SM	CL	2.8	-
3	CC 10 µm rad.	70	600	2	SM	CL	1.3	-
5	CC 9 µm rad.	78	1200	2	SM	CL	1.8	-
7	CC-E 18 µm rad.	70	600	2	MM	CL	0.22	-
8	CC-E 20 µm rad.	70	600	2	MM	CL	0.12	-
11	HC 14 µm core	90	750	7	SM	CL	3.2	-
12	HC 14 µm core	101	750	7	SM	CL	2.5	-
18	DL 14 µm sep.	101	100	14	-	-	-	-
19	DL 16 µm sep.	101	100	16	-	-	-	-
20	DL 20 µm sep.	101	100	20	-	-	-	-
23	DL-RC 14 µm sep.	101	500/100	7	SM	-	7.7	-
24	DL-RC 16 µm sep.	101	500/100	7	SM	-	5.7	-
27	CC 6 µm rad.	70	600	2	SM	CL	5.2	-
28	CC 7 µm rad.	70	600	2	SM	CL	2.8	-
29	CC 8 µm rad.	70	600	2	SM	CL	2.3	-
30	DL-RC 14 µm sep.	101	500/100	7	SM	CL	4.7	-
31	DL-RC 14 µm sep.	101	500/100	7	SM	CL	9.3	-

Table 2. Writing parameters, type of guided modes and upper limit for the propagation losses for sample 2. The facet used for the waveguide inscription is specified in brackets together with the waveguide number. Abbreviations are the same of Table 1.

WG	Description	E [nJ]	V [µm/s]	T [µm]	Modes		α [dB/cm]	
					π	σ	π	σ
1(a)	CC 8 µm rad.	90	600	2	SM	CL	6.8	-
2(a)	CC 9 µm rad.	90	600	2	SM	CL	4.1	-
3(a)	CC 10 µm rad.	90	600	2	SM	CL	2.2	-
8(a)	CC-E 20 µm rad.	90	600	2	MM	CL	0.19	-
9(a)	CC-E 18 µm rad.	106	1200	2	MM	CL	0.30	-
12(a)	HC 14 µm core	115	750/100	7	SM	CL	2.5	-
13(a)	DL-RC 14 µm sep.	115	750/100	7	SM	-	3.9	-
14(a)	DL-RC 16 µm sep.	115	750/100	7	SM	-	4.7	-
19(a)	SL	80	500	-	-	SM	-	5.3
1(c)	CC 8 µm rad.	78	600	2	SM	CL	5.3	-
5(c)	CC 9 µm rad.	92	1200	2	SM	CL	3.8	-
6(c)	CC 10 µm rad.	92	1200	2	SM	CL	3.7	-
7(c)	CC-E 18 µm rad.	92	1200	2	MM	CL	0.38	-
8(c)	CC-E 20 µm rad.	92	1200	2	MM	CL	0.34	-
10(c)	HC 14 µm core	101	750	7	SM	CL	3.9	-
11(c)	DL-RC 14 µm sep.	101	750	7	SM	-	4.9	-
12(c)	DL-RC 16 µm sep.	101	750	7	SM	-	5.5	-
15(c)	SL	73	500	-	-	SM	-	5.7

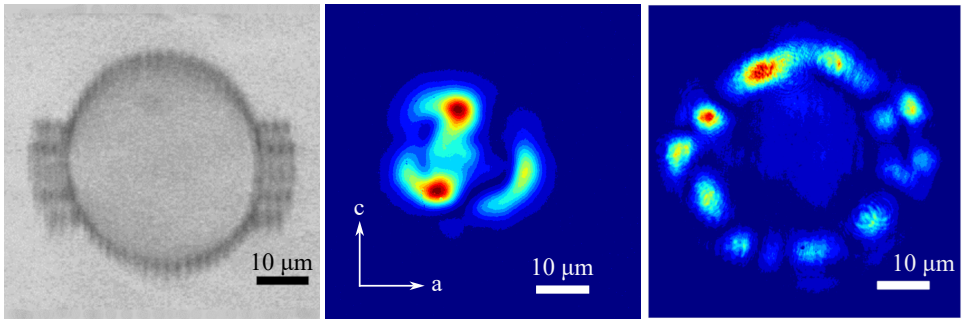

(**a**) Microscope image of WG7 (**b**) WG7 π-pol, 632.8 nm (**c**) WG7 σ-pol, 632.8 nm

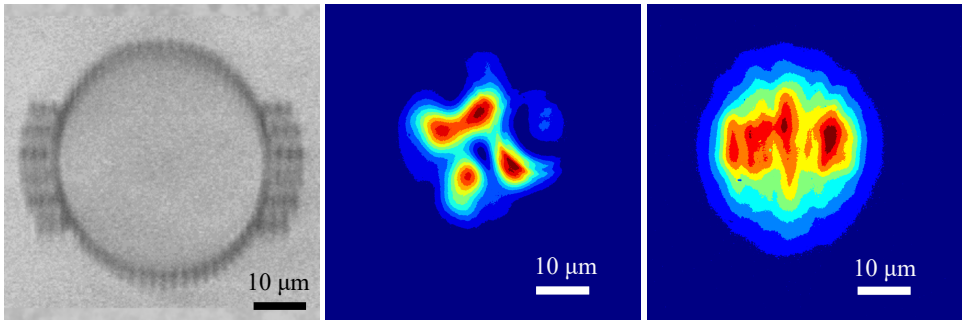

(**d**) Microscope image of WG8 (**e**) WG8 π-pol, 632.8 nm (**f**) WG8 π-pol, 444 nm

Figure 3. Microscope images of the end facets of the waveguides (**a**,**d**) and near-field pictures for WG7 (**b**,**c**) and WG8 (**e**,**f**) of sample 1. The orientation of crystallographic axes reported in the figure (**b**) is common to all pictures. Near-field profiles have been registered adjusting the position of the input beam in order to obtain the maximum output power.

To estimate the refractive index reduction in the irradiated area for π-polarization, a measurement of the numerical aperture of the waveguide has been performed. The waveguide chosen was WG8 of sample 1, due to the greater transmission efficiency and thus, less scattered light on the beam profiler. Through the step index waveguide approximation [11], it is possible to connect the numerical aperture to the refractive index difference between core and cladding. The obtained value for Δn is 2×10^{-4}.

To identify the waveguides suitable for lasing, coupling and transmission measurements have been performed also at 444 nm. The chosen source was an InGaN-based laser diode tuned to emit at 444 nm in order to match the absorption peak of Pr^{3+} ions. A collimation lens was used to collect the beam exiting from the laser diode and then a couple of cylindrical lenses (Schäfter+Kirchhoff 5 AN-3-V-35) was used to reduce the beam astigmatism. Since the laser diode emission is mainly polarized, a half wavelength plate and a polarizing beam splitter were used to control the pump power, keeping constant the emission wavelength of the diode. A second half wavelength plate was employed to control the beam polarization, in order to study both σ and π polarization at this wavelength. The maximum available power before the focusing lens was about 1.7 W. The best performance has been observed employing as coupling lens the same achromatic lens of 30 mm focal length employed for the 632.8 nm wavelength. The focused beam has been studied with the BP. The beam had a diameter of 60 µm with a corresponding value of M_x^2 of 20 in the horizontal direction and a diameter of 40 µm with an M_y^2 of 1.7 for the vertical direction. The definition of M_x^2 and M_y^2 is the one reported in the ISO 11146-1:2021 standard. The choice of a pump beam wider than the average dimension of the waveguide is due to the numerical aperture of the waveguides (about 0.04), which limits the divergence of the input beam. The chosen lens was found to be the best compromise between beam diameter and divergence.

SL waveguides do not show any confinement for both polarizations, while DL waveguides and DL-RC waveguides confine only π polarization at the pump wavelength, with a transmission efficiency of a few percent, once the praseodymium absorption is subtracted. Waveguides which shows the best performance are the depressed cladding ones. These waveguides confine π polarization in the core and for some designs (CC-E and HC structures), σ polarization is also confined in the core but with transmission efficiencies of about 1–4%. All the waveguides which confine the radiation were found to be multimodal. As already observed at 632.8 nm, the best results were achieved with the CC-E waveguides. A summary of the transmission efficiencies measured for these waveguides is reported in Table 3. Observing the results of the coupling measurements, we expected π-polarized lasing from the waveguides given the lower propagation losses of this polarization with respect to σ polarization.

A phenomenon noted during the measurements is the increase in the transmission efficiency when increasing the incident power on the waveguide. A possible explanation of this effect is related to the presence of praseodymium ions whose absorption spectrum has a peak at 444.0 nm for π polarization, as reported in Figure 1. The transition involved in the absorption process is the $^3H_4 \rightarrow {}^3P_2$. This last manifold quickly decays via phonon-assisted transition to the $^3P_0$, a metastable level with a mean lifetime of about 45 µs [3]. The high pump power together with the spatial confinement induced by the presence of the waveguide leads to a radiation intensity of approx. 100 kW/cm^2, and saturation of the absorption of the active medium in the waveguide can occur, due to the depletion of the ground state. The same effect has been reported for femtosecond-laser-written waveguides in Tm:$KLu(WO_4)_2$ [11]. A simple modelization of this effect can be achieved with a rate equation system and it is reported in Appendix A. The obtained relation between the incident power on the waveguide facet (P_{INC}) and the output power (P_{OUT}) is given by:

$$P_{OUT} = F_{OUT} P_S \omega \left(\frac{\eta_{CL} F_{IN} P_{INC}}{P_S} - Q + \ln\left(\frac{\eta_{CL} F_{IN} P_{INC}}{P_S} \right) \right) \quad (1)$$

where ω is the Wright omega function, and F_{IN} and F_{OUT} are the Fresnel losses at the two interfaces between air and LLF.

Table 3. Transmission efficiency for π polarized radiation at 444 nm for the circular cladding waveguides "with ears".

Sample	WG	Radius [μm]	T_π [%]
1	7	18	34
	8	20	42
	9	18	29
	10	20	36
2	7 a-cut	18	27
	8 a-cut	20	35
	9 a-cut	18	25
	10 a-cut	20	32
	7 c-cut	18	32
	8 c-cut	20	35

This model has three parameters: η_{CL} is the coupling efficiency of the waveguide for the pump beam, P_S is an effective saturation power and Q is connected to the low-intensity absorption coefficient, directly measured by transmission measurement with the unfocused laser diode light through the bulk crystal, subtracting the effect of the Fresnel losses. In this case, no violations of the linear trend are observed, due to the larger beam diameter, about 1 mm, with respect to the waveguide diameter. The values of the other two parameters are derived from the best fit of the transmission data. The measurements have been carried out on three waveguides of different diameters, WG3, WG7 and WG8 of sample 1, in order to study this effect with waveguides of different diameter, namely 20 μm, 36 μm and 40 μm. A best fit with the model reported in Equation (1) has been performed. The results of the best fit for the three waveguides are reported in Table 4, while the data and the best fit plot are reported in Figure 4a–c. In the figures, P_{INC} is the incident power while P_{OUT} is the output power from the waveguide.

Table 4. Best fit parameters obtained for the three waveguides.

WG	P_S [W]	η_{CL} [%]
3	0.09	12
7	0.40	35
8	0.56	44

As expected, the value of P_S is greater for larger waveguides. To exploit the dependence on the area of the waveguide, a linear fit is performed between the area of the waveguide (A) and the saturation power obtained from the best fit. The model used is:

$$P_S = \hat{I}_S A + P_0 \quad (2)$$

where P_0 is an additional parameter to compensate the effect of the approximations made.

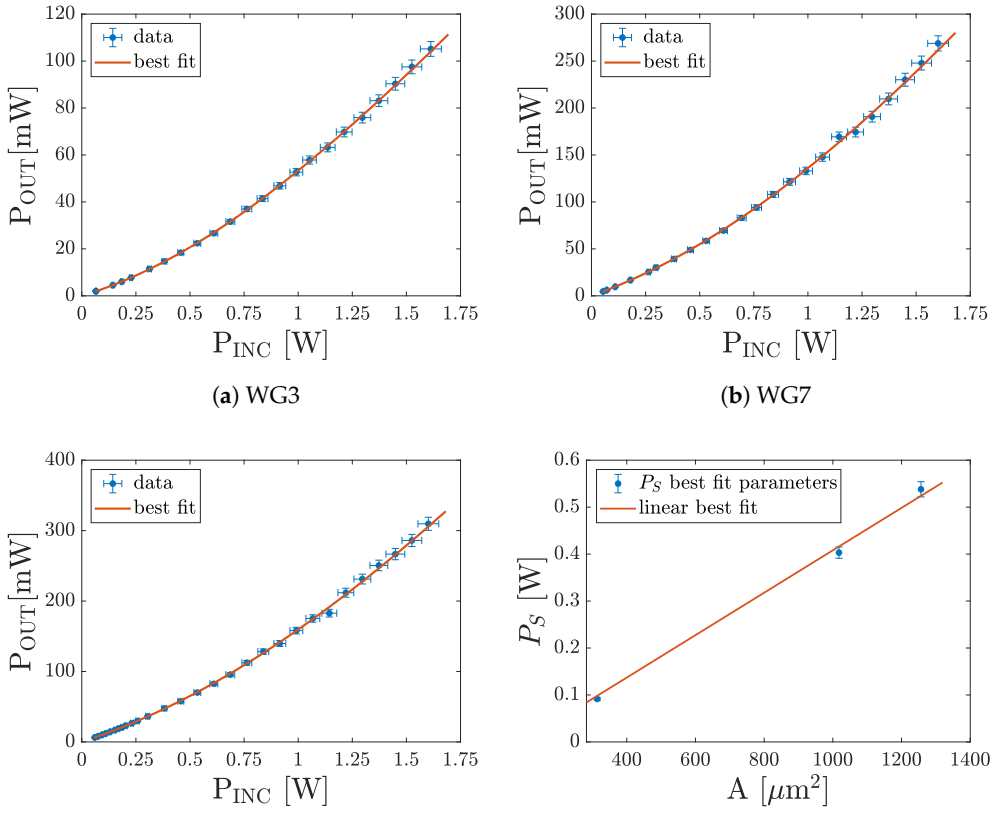

(**a**) WG3 (**b**) WG7

(**c**) WG8 (**d**) Linear fit

Figure 4. (**a**–**c**) Transmission data and best fit for the three waveguide analyzed. (**d**) Linear fit of the P_S best fit parameters for the three waveguides.

The obtained result is $\hat{I}_S = 50\,\mathrm{kW/cm^2}$ and $P_0 = -0.05\,\mathrm{W}$. Data and best fit are presented in Figure 4d. The assumed linear trend is found in the experimental data. The expected value for I_S can be derived from Equation (A9), assuming as value for the absorption cross section the one reported in [2], obtaining thus a value of $1.0\,\mathrm{GW/m^2}$. This value differs by a factor of two from the experimental one, but this is acceptable since the simplicity of the rate equation model considered and the approximations made, similar to the uniform distribution of the power in the core of the waveguide, not satisfied by the waveguides studied (see Figure 3f), where the output profile at maximum coupling efficiency is reported. With this method it is possible to isolate the coupling efficiency of the waveguide. The value of η_{CL} reported in Table 4 are compatible with the value of T_π shown in Table 3, and this corresponds to a low value of propagation losses, as indeed observed with the measurement reported in Table A2. The values of the coupling efficiency (<50%) are mainly due to the diameter mismatch between the waveguides and the pump beam, namely 20–40 µm and 60 µm. Since it is possible to estimate the coupling efficiency, both the threshold power and the slope efficiency of the realized lasers will be given with respect to the power coupled in the waveguide ($\eta_C = \frac{dP_{OUT}}{dP_c}$). Here P_{OUT} indicates the laser output power.

2.3. Cavity Design

The laser cavity we chose consists of two mirrors butt-coupled to the crystal facet. To this end, the mirrors were mounted in a two axes tilting stage as well as in a three axes translation system. A picture of the laser cavity is reported in Figure 5. The pump beam was focused with the 30 mm focal length lens employed for the coupling measurements. The input coupler possesses high transmittance at the pump wavelength (>98%) and high reflectance in the orange region (T = 0.1% at 604 nm) and $T < 10^{-5}$ for $630\,\mathrm{nm} < \lambda < 740\,\mathrm{nm}$,

covering all the red and deep red emission of Pr^{3+} ions. Four different output couplers were employed for the laser experiments and their characteristics are reported in Table 5:

Table 5. Summary of the characteristics of the employed mirrors. The transmittance values were measured with the CARY 5000 spectrophotometer.

Mirror	R [mm]	Transmittance [%] at λ [nm]			
		604	**645**	**698**	**721**
1	plane	77	0.8	0.03	0.05
2	plane	16	96	58	71
3	plane	96	74	69	46
4	50	75	7	0.9	0.8

Mirror 1 possesses high reflectance in the deep red region and was used to test the possibility of starting laser operation due to the lower threshold expected from the low extraction of the mirror. Mirror 2 was employed to study the operation in the orange region, with an extraction of about 16%. Finally, mirrors 3 and 4 were chosen to study the laser behavior in the deep red region, increasing the extraction of the output coupler. In particular, mirror 3 possesses an extraction of 96% at 604 nm in order to suppress parasitic lasing at this wavelength while employing higher extraction in the deep red region. Laser radiation has been collected with an achromatic lens of 20 mm of focal length and a 510 nm long-pass dielectric filter has been used to remove the residual pump from the beam. During the laser experiments, the crystal was cooled to 12 °C to avoid overheating under blue light pumping. Laser emission spectrum has been measured with a QEpro spectrophotometer.

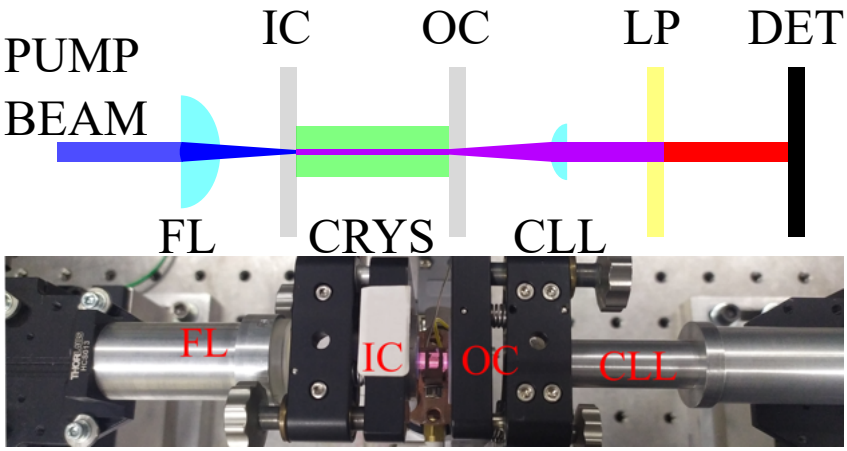

Figure 5. Schematic representation of the setup employed for the experiments (**above**) and a picture of the laser cavity (**below**). The waveguide is visible due to the fluorescence emitted under blue light pumping. Abbreviations: FL: focusing lens, IC: input coupler, CRYS: crystal, OC: output coupler, CLL: collection lens, LP: long pass dielectric filter, DET: power meter.

3. Results

The first experiment we performed was to check the possibility of laser oscillation within the waveguide, employing as output coupler mirror 1. Lasing was observed in many waveguides and a summary of the results obtained with the ear-like waveguides is reported in Table 6.

Table 6. Summary of laser obtained with the waveguides with the ears using as output coupler mirror 1.

Sample	WG	Radius [μm]	λ [nm]	T_{OC} [%]	P_{OUT} [mW]
1	7	18	604	77	63
	8	20	698	0.03	3.0
	9	18	604	77	50
	10	20	721	0.05	1.0
2	7 a-cut	18	721	0.05	1.0
	8 a-cut	20	721	0.05	1.5
	9 a-cut	18	721	0.05	0.9
	10 a-cut	20	721	0.05	1.0
	7 c-cut	18	721	0.05	1.0
	8 c-cut	20	721	0.05	1.2

As expected, most of the waveguides operate at 721 nm, due to the greater emission cross section [2]. On the contrary, waveguides WG7 and WG9 of sample 1 operate at 604 nm despite the high extraction of the mirror (77%). We hypothesized that this effect could be due to the different overlap efficiency between the pump modes and the laser modes, which favors the orange wavelength with respect to the deep red ones. In our opinion, this observation could be connected to the smaller diameter and the lower pulse energy used to write these waveguides in sample 1 with respect to those used for the second one (see Tables A1 and A2), where only lasing at 721 nm was observed. A more interesting result has been achieved with WG8 of sample 1. Employing mirror 1, we achieved stable continuous-wave lasing at 698 nm, corresponding to one of the lines necessary for the operation of the atomic clock based on neutral strontium atom [6]. This is, to the best of our knowledge, the first demonstration of a Pr-based waveguide laser operating at this wavelength. Laser threshold and slope efficiency were measured obtaining values of 0.46% for η_c and 25 mW for P_{THR}. The maximum power obtained is 3 mW. Data and linear fit are shown in Figure 6. The low values reported for the maximum output power and for the slope efficiency are due to the low transmission of the OC, which is necessary because of the lower emission cross section of the $^3P_0 \rightarrow {}^3F_3$ transition with respect to that of the $^3P_0 \rightarrow {}^3F_4$ transition [2] leading to the difficulty of reaching free running laser emission at this wavelength with a broadband mirror, due to the competition with a transition of larger emission cross section. In our hypothesis, the better overlap efficiency of the confined modes at 698 nm with the confined pump beam favors this wavelength with respect to the 721 nm one. The emission mode is a high quality mode composed by a single lobe with M_x^2 and M_y^2 of 1.5 and 1.9, respectively.

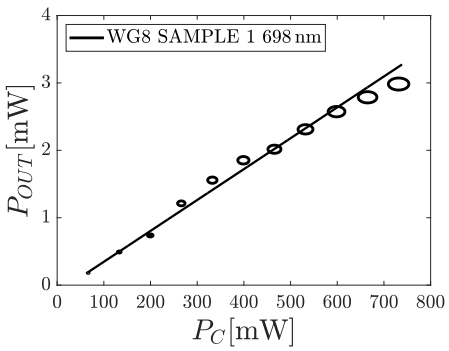

Figure 6. Data and best fit 698 nm laser emission. For each point, the dimension of the marker corresponds to the relative error bar.

Once the possibility of starting laser emission from the waveguides is verified, we substituted the output coupler with the other three mirrors, in order to increase the output power for the emissions in the orange (mirror 2), and in the deep red (mirrors 3 and 4). For each sample, the best results in terms of output power and slope efficiency are reported in Table 7, while data and best-fitting lines are reported in Figure 7a,b.

Table 7. Comparison between the best laser result obtained in each sample. The best overall results for each wavelength are shown in bold.

λ [nm]	WG	T_{OC} [%]	η_c [%]	P_{THR} [mW]	P_{MAX} [mW]
604	WG8(1)	16	16	100	**86**
	WG8 (2 a-cut)	16	14	140	56
	WG7(1)	77	**26**	310	63
721	WG8(1)	46	14	280	60
	WG8 (2 a-cut)	46	**18**	150	**70**

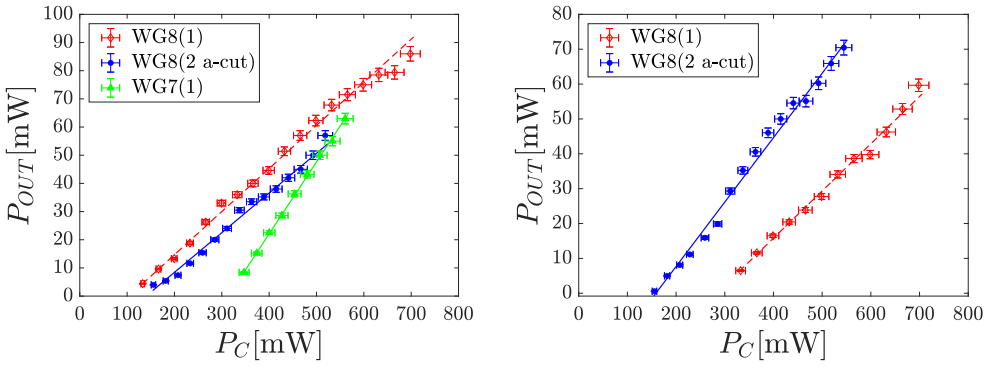

(**a**) 604 nm (**b**) 721 nm

Figure 7. Data and best-fitting lines of the best results in each sample.

Concerning the emission at 604 nm, best results were observed in sample 1, where a maximum output power of 86 mW was observed in WG8 with mirror 2. Employing the same mirror with sample 2, slightly lower efficiency was measured in WG8 of the a-cut facet and the maximum output power was also limited at 56 mW by a lower coupling efficiency of the pump beam. The maximum slope efficiency of 26% was observed in WG7 of sample 1 using mirror 1 as the output coupler, with a transmission of 77%. The higher transmission translates in a higher slope efficiency but also in a higher laser threshold, about 300 mW, compared to those observed for the other two waveguides described in Table 7, about 100 mW. None of the waveguides written in sample 2 showed lasing at 604 nm with mirror 1, operating instead at 721 nm, as reported in Table 6.

An opposite situation can be observed for the emission at 721 nm.; Further, in this case, the best results in sample 2 were obtained with WG8 a-cut, which presents higher efficiency (18%) and output power (70 mW) with respect to those obtained in waveguide WG8 of sample 1, although with a lower coupling efficiency. Moreover, waveguide WG8 of the first sample presents a higher threshold power, 280 mW instead of 150 mW) with the same mirror (mirror 3). As stated before, the different behavior of the waveguides can be connected to the different overlap efficiencies between the pump beam and the modes at the laser wavelengths, strongly dependent on the writing parameters such as pulse energy and translation velocity employed for waveguide fabrication. The highest values of output power reported in Table 7 are higher than the values reported previously in literature, to the best of our knowledge, for femtosecond-written waveguide lasers realized in praseodymium-doped fluoride crystals.

Operating the laser cavity with mirror 4, WG7 of sample 1 demonstrated laser operation at 645 nm at maximum pump power ($P_C \approx 500$ mW), with an output power of about 1 mW. Reducing the pump power, the operation wavelength changes to 604 nm. This phenomenon is due to the absorption of 604 nm radiation by Pr ions caused by the presence of the $^3H_4 \rightarrow {}^1D_2$ transition. The $^1D_2$ manifold has a mean lifetime of about 360 µs [26] and the presence of the laser mode contributes to the depletion of the ground state due to an effect similar to the one described in Appendix A. The depletion of the ground state is greater when rising the output power of the laser and this reflects in a reduction in the pump absorption, and thus the maximum gain the active medium can reach. On the contrary, emission at 645 nm does not suffer from this reabsorption effect but the lower emission cross section [2] suppresses this wavelength at lower pump power. Due to the wavelength change, it was not possible to measure the slope efficiency of the laser operating at this wavelength. The emission spectrum is reported in Figure 8. This is the first demonstration of lasing at this wavelength in a praseodymium-based waveguide laser.

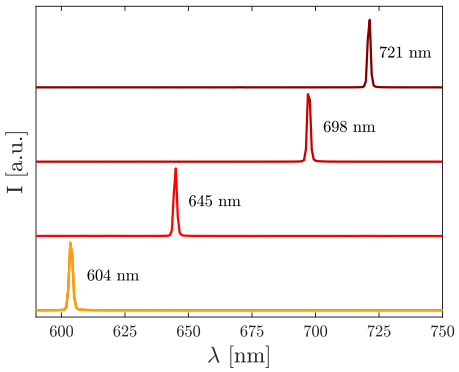

Figure 8. Spectra of the laser emission described in this work.

For each of the observed wavelengths, the intensity profile of the laser emission of the best result in terms of output power is shown in Figure 9. In addition to the presented results, lasing at 721 nm has been observed, employing mirror 1 as output coupler, in all the circular waveguides with radius between 8 µm and 10 µm. Output power was limited in the 100 µW–400 µW range from the high reflectivity of the OC and the low power coupled in the waveguide; see Table 4. All the observed laser emissions are π-polarized.

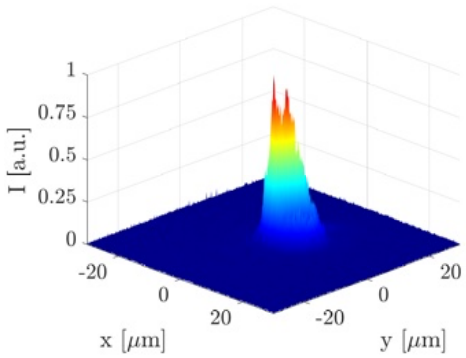

(**a**) WG8 sample 1 at 604 nm

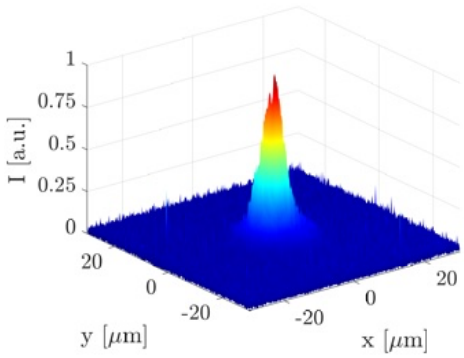

(**b**) WG8 sample 1 at 698 nm

Figure 9. *Cont.*

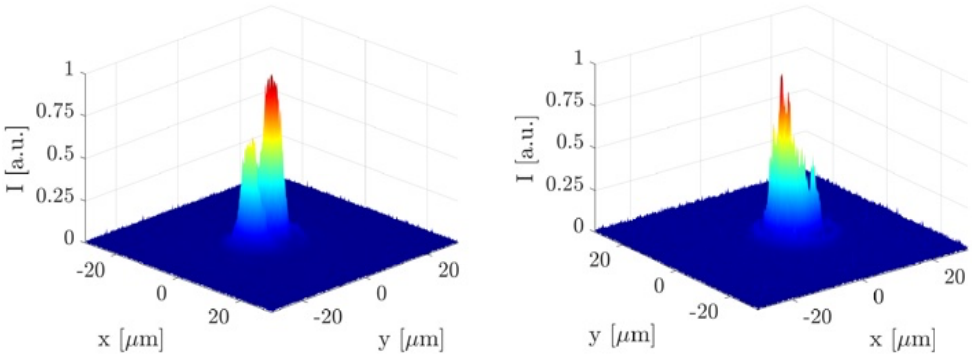

(**c**) WG8 sample 2 a−cut at 721 nm (**d**) WG7 sample 1 at 604 nm

Figure 9. Intensity profiles of the laser emission at various wavelengths. The intensity profiles were taken at maximum output power.

4. Conclusions

In this work, we reported the first operation of a femtosecond-laser-written waveguide visible laser based on Pr:LLF. Several structures were tested and the waveguide design was optimized to obtain a low-loss depressed cladding waveguide showing propagation losses of 0.12 dB/cm, comparable to those obtained for ultra-large area waveguides in YLF [16]. Laser emission has been obtained at 604 nm and 721 nm, reaching output powers greater than those reported in the literature for standard-area waveguides in praseodymium-doped fluoride crystals [14,15], a result achieved by the use of high quality material and a meticulously designed depressed cladding waveguide. Higher output power has been achieved at 604 nm in ultra-large area waveguides but this type of structures operates with worse quality emission modes.

Moreover, we obtained continuous wave laser operation at 698 nm, corresponding to the wavelength necessary for the operation of the atomic clock based on neutral strontium atom. Although the output power achieved is lower than the values obtained in Pr:LLF based bulk lasers [2], the power necessary for metrological devices is only of a few milliwatts [5,6]. Output power at 698 nm was limited by the extraction of the output coupler and power scaling of the laser device can be easily obtained with a mirror specifically designed to suppress the emission at wavelengths corresponding to greater emission cross sections.

Finally, we achieved stable laser operation at 645 nm. This wavelength can be employed for ammonia gas sensing [27] and a waveguide laser operating at this wavelength could be used as light source in compact gas sensing systems, obtaining a device with a greater mean lifetime with respect to laser diodes. These two last wavelengths have never been reported previously in the existing literature for praseodymium-based waveguide lasers. An improvement of the stability and miniaturization of the whole system can be reached substituting the mirrors with partially reflective coating deposited on crystal facets. Although the values of the output power presented in this article are lower than the results obtained in praseodymium-based bulk lasers, the design of a cavity employing a waveguide could lead to a device with a reduced number of refractive elements, such as birefringent plates and etalons, when compared to a bulk laser. This corresponds to greater frequency stability of the whole device, opening the door to compact metrological sources, where a few tens of milliwatts of output power are required.

Author Contributions: Investigation, D.B., I.L.-Q., J.R.V.d.A., M.T. and A.T.; Waveguide design and fabrication, I.L.-Q. and J.R.V.d.A.; writing—original draft preparation, D.B., I.L.-Q., J.R.V.d.A., M.T. and A.T.; writing—review and editing, D.B., I.L.-Q., J.R.V.d.A., M.T. and A.T. All authors have read and agreed to the published version of the manuscript.

Funding: Consejería de Educación, Junta de Castilla y León (SA136P20); Ministerio de Ciencia, Innovación y Universidades (PID2020-119818).

Institutional Review Board Statement: Not applicable.

Informed Consent Statement: Not applicable.

Data Availability Statement: Data underlying the results presented in this paper are not publicly available at this time but may be obtained from the authors upon reasonable request.

Acknowledgments: The authors would like to acknowledge E. Damiano, G. Cittadino and F. Caminati for the helpful discussions and I. Grassini for her care and competence in preparing the samples.

Conflicts of Interest: The authors declare no conflict of interest.

Abbreviations

The following abbreviations are used in this manuscript:

SSL	Solid State Laser
ST	Single Track
DL	Stress-induced double-line
DL-RC	Stress-induced double-line with rhombic cladding
CC	Circular cladding
CC-E	Circular cladding with "ear-like" structures
HC	Hexagonal cladding

Appendix A. Model Derivation

For this simple model, schematized in Figure A1, three manifolds of praseodymium ion are considered, the fundamental, $^3H_4$, the pump manifold, $^3P_2$ and the upper laser level, $^3P_0$. The rate equations for the system are:

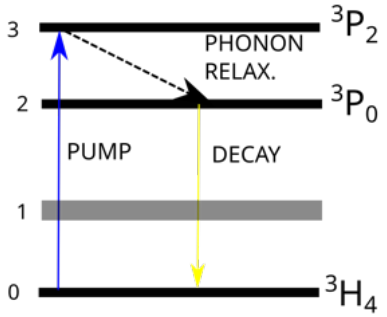

Figure A1. Schematic representation of the rate equation model.

$$\frac{dN_3}{dt} = \sigma_{abs}\frac{I_P}{h\nu_p}N_0 - \frac{N_3}{\tau_3} - \sigma_{em}\frac{I_P}{h\nu_p}N_3 \tag{A1}$$

$$\frac{dN_2}{dt} = \frac{N_3}{\tau_3} - \frac{N_2}{\tau_2} \tag{A2}$$

$$\frac{dN_0}{dt} = -\sigma_{abs}\frac{I_P}{h\nu_p}N_0 + \frac{N_2}{\tau_2} + \sigma_{em}\frac{I_P}{h\nu_p}N_3 \tag{A3}$$

where N_3 is the population density of $^3P_2$ manifold, N_2 is that of the $^3P_0$ level and N_0 is the population density of the $^3H_4$ manifold, with the condition $N_0 + N_2 + N_3 = N_{TOT}$, total concentration of praseodymium ions; σ_{abs} and σ_{em} are, respectively, the absorption and emission cross sections, I_P is the pump radiation intensity and $h\nu_p$ is the pump photon energy. τ_3 is the lifetime of the pump level and τ_2 the one of the upper laser level.

An approximation made in writing these equations is that population in the upper laser level decays directly to the fundamental level, instead of decaying to the lower laser levels. In fact, ions in the $^3P_0$ level also decay to the ^3F_J manifold and to the other levels of

the ^3H_J manifold [3]. Those levels act as lower laser levels in praseodymium-based solid state lasers working in the wavelength range from 500 nm to 730 nm [2].

Those levels, collectively indicated as 1 in Figure A1, have shorter lifetimes with respect to the upper laser level one, so the approximation of completely depleted levels can hold, allowing the approximation made in writing the number conservation condition as $N_0 + N_2 + N_3 = N_{TOT}$. The steady state solution of Equations (A1)–(A3) is, substituting $E = h\nu_p$:

$$N_0 = \frac{\mathrm{E} + I_P\sigma_{\mathrm{em}}\tau_3}{\mathrm{E} + I_P\sigma_{\mathrm{em}}\tau_3 + I_P\sigma_{\mathrm{abs}}\tau_2 + I_P\sigma_{\mathrm{abs}}\tau_3} N_{TOT} \tag{A4}$$

$$N_1 \approx 0 \tag{A5}$$

$$N_2 = \frac{I_P\sigma_{\mathrm{abs}}\tau_2}{\mathrm{E} + I_P\sigma_{\mathrm{em}}\tau_3 + I_P\sigma_{\mathrm{abs}}\tau_2 + I_P\sigma_{\mathrm{abs}}\tau_3} N_{TOT} \tag{A6}$$

$$N_3 = \frac{I_P\sigma_{\mathrm{abs}}\tau_3}{\mathrm{E} + I_P\sigma_{\mathrm{em}}\tau_3 + I_P\sigma_{\mathrm{abs}}\tau_2 + I_P\sigma_{\mathrm{abs}}\tau_3} N_{TOT} \tag{A7}$$

This approximation can be also performed on the pump manifold, since the condition $\tau_3/\tau_2 << 1$ is satisfied, due to the quenching of the $^3P_2$ levels by phonon-assisted transitions. Neglecting the terms proportional to τ_3/τ_2, the variation of radiation intensity during propagation can be written as:

$$\frac{dI}{dz} = -N_{TOT}\sigma_{abs}\frac{1}{1+\frac{I}{I_S}}I = -\alpha_0\frac{1}{1+\frac{I}{I_S}}I \tag{A8}$$

where:

$$I_S = \frac{h\nu}{\tau_2\sigma_{abs}} \tag{A9}$$

is called saturation intensity. Writing Equation (A8), plane wave approximation is assumed to describe the radiation propagating in the material.

The solution of Equation (A8) for the propagation in a medium with thickness L and with an incident intensity of radiation I_0 is:

$$I(L) = I_S\omega\left(\frac{I_0}{I_S} - Q + \ln\left(\frac{I_0}{I_S}\right)\right) \tag{A10}$$

where W_0 is the Lambert function, ω is the Wright omega function and $Q = \alpha_0 L$.

To apply these calculations to the waveguides, the intensity distribution within the waveguide is approximated as uniform, connecting thus the power and the intensity of radiation with a surface factor. The value of P_0 is connected to the incident power by the coupling efficiency, indicated as η_{CL}. Substituting the radiation intensity with the power propagating in the waveguide, and expressing the output power as a function of the incident power, relation (A10) becomes:

$$P_{OUT} = P_S\omega\left(\frac{\eta_{CL}P_{INC}}{P_S} - Q + \ln\left(\frac{\eta_{CL}P_{INC}}{P_S}\right)\right) \tag{A11}$$

Including the effect of Fresnel losses, the model derived becomes the one reported in Equation (1).

Appendix B. Summary of the Results for All the Waveguides

In this section, we report the results of the coupling and transmission measurements with the 632.8 nm radiation for each of the written waveguides, as well as the writing parameters. In the following tables, E is the pulse energy on the sample, V is the scan velocity and T is the track separation.

Table A1. Writing parameters, type of guided modes and upper limit for the propagation losses for sample 1. SM means single mode waveguide, MM stands for multimodal waveguide, CL is for a mode confined in the cladding and not in the core while - is a non-confined polarization. The upper limit for the losses is reported only when the radiation is confined in the core of the waveguide.

WG	Description	E [nJ]	V [µm/s]	T [µm]	Modes		α [dB/cm]	
					π	σ	π	σ
1	CC 8 µm rad.	70	600	2	SM	CL	2.8	-
2	CC 9 µm rad.	70	600	2	SM	CL	2.8	-
3	CC 10 µm rad.	70	600	2	SM	CL	1.3	-
4	CC 8 µm rad.	78	1200	2	SM	CL	3.5	-
5	CC 9 µm rad.	78	1200	2	SM	CL	1.8	-
6	CC 10 µm rad.	78	1200	2	SM	CL	1.5	-
7	CC-E 18 µm rad.	70	600	2	MM	CL	0.22	-
8	CC-E 20 µm rad.	70	600	2	MM	CL	0.12	-
9	CC-E 18 µm rad.	78	1200	2	MM	CL	0.41	-
10	CC-E 20 µm rad.	78	1200	2	MM	CL	1.2	-
11	HC 14 µm core	90	750	7	SM	CL	3.2	-
12	HC 14 µm core	101	750	7	SM	CL	2.5	-
13	HC 14 µm core	90	750	7	SM	CL	3.3	-
14	HC 14 µm core	101	750	7	SM	CL	3.9	-
15	DL 14 µm sep.	90	100	14	-	-	-	-
16	DL 16 µm sep.	90	100	16	-	-	-	-
17	DL 20 µm sep.	90	100	20	-	-	-	-
18	DL 14 µm sep.	101	100	14	-	-	-	-
19	DL 16 µm sep.	101	100	16	-	-	-	-
20	DL 20 µm sep.	101	100	20	-	-	-	-
21	DL-RC 14 µm sep.	101	500/100	7	-	-	-	-
22	DL-RC 16 µm sep.	101	500/100	7	-	-	-	-
23	DL-RC 14 µm sep.	101	500/100	7	SM	-	7.7	-
24	DL-RC 16 µm sep.	101	500/100	7	SM	-	5.7	-
25	CC 6 µm rad.	70	600	2	SM	CL	11	-
26	CC 7 µm rad.	70	600	2	SM	CL	10	-
27	CC 6 µm rad.	70	600	2	SM	CL	5.2	-
28	CC 7 µm rad.	70	600	2	SM	CL	2.8	-
29	CC 8 µm rad.	70	600	2	SM	CL	2.3	-
30	DL-RC 14 µm sep.	101	500/100	7	SM	CL	4.7	-
31	DL-RC 14 µm sep.	101	500/100	7	SM	CL	9.3	-
32	HC 14 µm core	90	750/100	7	SM	CL	13	-

Table A2. Writing parameters, type of guided modes and upper limit for the propagation losses for sample 2. The facet used for the waveguide inscription is specified nearby the number of the waveguide. Abbreviations are the same of Table A1.

WG	Description	E [nJ]	V [µm/s]	T [µm]	Modes		α [dB/cm]	
					π	σ	π	σ
1(a)	CC 8 µm rad.	90	600	2	SM	CL	6.8	-
2(a)	CC 9 µm rad.	90	600	2	SM	CL	4.1	-
3(a)	CC 10 µm rad.	90	600	2	SM	CL	2.2	-
4(a)	CC 8 µm rad.	106	1200	2	SM	CL	7.2	-
5(a)	CC 9 µm rad.	106	1200	2	SM	CL	5.5	-
6(a)	CC 10 µm rad.	106	1200	2	SM	CL	2.3	-
7(a)	CC-E 18 µm rad.	90	600	2	MM	CL	0.38	-
8(a)	CC-E 20 µm rad.	90	600	2	MM	CL	0.19	-
9(a)	CC-E 18 µm rad.	106	1200	2	MM	CL	0.30	-
10(a)	CC-E 20 µm rad.	106	1200	2	MM	CL	0.19	-
11(a)	HC 14 µm core	115	750/100	7	SM	CL	3.0	-
12(a)	HC 14 µm core	115	750/100	7	SM	CL	2.5	-
13(a)	DL-RC 14 µm sep.	115	750/100	7	SM	-	3.9	-
14(a)	DL-RC 16 µm sep.	115	750/100	7	SM	-	4.7	-
15(a)	SL	98	500	-	-	SM	-	8.7
16(a)	SL	98	150	-	-	-	-	-
17(a)	SL	90	500	-	-	SM	-	6.9
18(a)	SL	98	150	-	-	SM	-	10
19(a)	SL	80	500	-	-	SM	-	5.3
20(a)	SL	80	150	-	-	SM	-	7.2
1(c)	CC 8 µm rad.	78	600	2	SM	CL	5.3	-
2(c)	CC 9 µm rad.	78	600	2	SM	CL	4.3	-
3(c)	CC 10 µm rad.	78	600	2	SM	CL	4.4	-
4(c)	CC 8 µm rad.	92	1200	2	SM	CL	9.6	-
5(c)	CC 9 µm rad.	92	1200	2	SM	CL	3.8	-
6(c)	CC 10 µm rad.	92	1200	2	SM	CL	3.7	-
7(c)	CC-E 18 µm rad.	92	1200	2	MM	CL	0.38	-
8(c)	CC-E 20 µm rad.	92	1200	2	MM	CL	0.34	-
9(c)	HC 14 µm core	101	750	7	SM	CL	4.2	-
10(c)	HC 14 µm core	101	750	7	SM	CL	3.9	-
11(c)	DL-RC 14 µm sep.	101	750	7	SM	-	4.9	-
12(c)	DL-RC 16 µm sep.	101	750	7	SM	-	5.5	-
13(c)	SL	84	500	-	-	SM	-	6.2
14(c)	SL	84	150	-	-	SM	-	16
15(c)	SL	73	500	-	-	SM	-	5.7
16(c)	SL	73	150	-	-	SM	-	7.3
17(c)	SL	62	500	-	-	-	-	-
18(c)	SL	62	150	-	-	-	-	-
19(c)	SL	50	500	-	-	-	-	-
20(c)	SL	50	150	-	-	-	-	-

References

1. Matthey, R.; Affolderbach, C.; Mileti, G. Methods and evaluation of frequency aging in distributed-feedback laser diodes for rubidium atomic clocks. *Opt. Lett.* **2011**, *36*, 3311–3313. [CrossRef] [PubMed]
2. Kränkel, C.; Marzahl, D.T.; Moglia, F.; Huber, G.; Metz, P.W. Out of the blue: semiconductor laser pumped visible rare-earth doped lasers. *Laser Photonics Rev.* **2016**, *10*, 548–568.
3. Cornacchia, F.; Richter, A.; Heumann, E.; Huber, G.; Parisi, D.; Tonelli, M. Visible laser emission of solid state pumped LiLuF4:Pr3+. *Opt. Express* **2007**, *15*, 992–1002. [CrossRef]
4. Sottile, A.; Damiano, E.; Lieto, A.D.; Tonelli, M. Diode-pumped solid-state laser platform for compact and long-lasting strontium-based optical clocks. *Opt. Lett.* **2019**, *44*, 594–597. [CrossRef]
5. Poli, N.; Schioppo, M.; Vogt, S.; Falke, S.; Sterr, U.; Lisdat, C.; Tino, G. A transportable strontium optical lattice clock. *Appl. Phys. B* **2014**, *117*, 1107–1116. [CrossRef]
6. Wang, Y.B.; Yin, M.J.; Ren, J.; Xu, Q.F.; Lu, B.Q.; Han, J.X.; Guo, Y.; Chang, H. Strontium optical lattice clock at the National Time Service Center. *Chin. Phys. B* **2018**, *27*, 023701. [CrossRef]
7. Davis, K.M.; Miura, K.; Sugimoto, N.; Hirao, K. Writing waveguides in glass with a femtosecond laser. *Opt. Lett.* **1996**, *21*, 1729–1731. [CrossRef]
8. Okhrimchuk, A.G.; Shestakov, A.V.; Khrushchev, I.; Mitchell, J. Depressed cladding, buried waveguide laser formed in a YAG:Nd3+ crystal by femtosecond laser writing. *Opt. Lett.* **2005**, *30*, 2248–2250. [CrossRef]
9. Okhrimchuk, A.; Mezentsev, V.; Shestakov, A.; Bennion, I. Low loss depressed cladding waveguide inscribed in YAG: Nd single crystal by femtosecond laser pulses. *Opt. Express* **2012**, *20*, 3832–3843. [CrossRef]
10. Sun, X.; Sun, S.; Romero, C.; de Aldana, J.R.V.; Liu, F.; Jia, Y.; Chen, F. Femtosecond laser direct writing of depressed cladding waveguides in Nd:YAG with "ear-like"; structures: fabrication and laser generation. *Opt. Express* **2021**, *29*, 4296–4307. [CrossRef]
11. Kifle, E.; Loiko, P.; Mateos, X.; de Aldana, J.R.V.; Ródenas, A.; Griebner, U.; Petrov, V.; Aguiló, M.; Díaz, F. Femtosecond-laser-written hexagonal cladding waveguide in Tm:KLu(WO4)2: μ-Raman study and laser operation. *Opt. Mater. Express* **2017**, *7*, 4258–4268. [CrossRef]
12. Morova, Y.; Tonelli, M.; Sennaroglu, A. Fabrication of femtosecond laser written depressed-cladding waveguides in Tm3+:BaY2F8 crystal and laser operation near 2 μm. *Opt. Mater.* **2022**, *126*, 112121. [CrossRef]
13. Calmano, T.; Paschke, A.G.; Müller, S.; Kränkel, C.; Huber, G. Curved Yb:YAG waveguide lasers, fabricated by femtosecond laser inscription. *Opt. Express* **2013**, *21*, 25501–25508. [CrossRef]
14. Müller, S.; Calmano, T.; Metz, P.; Hansen, N.O.; Kränkel, C.; Huber, G. Femtosecond-laser-written diode-pumped Pr:LiYF4 waveguide laser. *Opt. Lett.* **2012**, *37*, 5223–5225. [CrossRef] [PubMed]
15. Liu, H.; Luo, S.; Xu, B.; Xu, H.; Cai, Z.; Hong, M.; Wu, P. Femtosecond-laser micromachined Pr:YLF depressed cladding waveguide: Raman, fluorescence, and laser performance. *Opt. Mater. Express* **2017**, *7*, 3990–3997. [CrossRef]
16. Ren, Y.; Cui, Z.; Sun, L.; Wang, C.; Liu, H.; Cai, Y. Laser emission from low-loss cladding waveguides in Pr:YLF by femtosecond laser helical inscription. *Chin. Opt. Lett.* **2022**, *20*, 122201. [CrossRef]
17. Calmano, T.; Siebenmorgen, J.; Reichert, F.; Fechner, M.; Paschke, A.G.; Hansen, N.O.; Petermann, K.; Huber, G. Crystalline Pr:SrAl12O19 waveguide laser in the visible spectral region. *Opt. Lett.* **2011**, *36*, 4620–4622. [CrossRef]
18. Reichert, F.; Calmano, T.; Müller, S.; Marzahl, D.T.; Metz, P.W.; Huber, G. Efficient visible laser operation of Pr,Mg:SrAl12O19 channel waveguides. *Opt. Lett.* **2013**, *38*, 2698–2701. [CrossRef]
19. Calmano, T.; Sottile, A.; Metz, P.W.; Parisi, D.; Kränkel, C.; Tonelli, M.; Huber, G. Ultrafast Laser Inscribed Pr:KY3F10 Waveguides for Dual Wavelength and Switchable Waveguide Lasers in the Visible. In Proceedings of the Advanced Solid State Lasers, Berlin, Germany, 4–9 October 2015; Optica Publishing Group: Washington, DC, USA, 2015; p. AW1A.5. [CrossRef]
20. Kaminskii, A.A.; ichi Ueda, K.; Uehara, N. New Laser-Diode-Pumped CW Laser Based on Nd^{3+}-Ion-Doped Tetragonal $LiLuF_4$ Crystal. *Jpn. J. Appl. Phys.* **1993**, *32*, L586–L588. [CrossRef]
21. Aggarwal, R.L.; Ripin, D.J.; Ochoa, J.R.; Fan, T.Y. Measurement of thermo-optic properties of Y3Al5O12, Lu3Al5O12, YAIO3, LiYF4, LiLuF4, BaY2F8, KGd(WO4)2, and KY(WO4)2 laser crystals in the 80–300K temperature range. *J. Appl. Phys.* **2005**, *98*, 103514.
22. Chen, F.; de Aldana, J.R.V. Optical waveguides in crystalline dielectric materials produced by femtosecond-laser micromachining. *Laser Photonics Rev.* **2014**, *8*, 251–275.
23. Jia, Y.; Cheng, C.; Vázquez de Aldana, J.R.; Castillo, G.R.; Rabes, B.d.R.; Tan, Y.; Jaque, D.; Chen, F. Monolithic crystalline cladding microstructures for efficient light guiding and beam manipulation in passive and active regimes. *Sci. Rep.* **2014**, *4*, 5988. [CrossRef]
24. Burghoff, J.; Nolte, S.; Tünnermann, A. Origins of waveguiding in femtosecond laser-structured $LiNbO_3$. *Appl. Phys. A* **2007**, *89*, 127–132. [CrossRef]
25. Cheng, C.; Jia, Y.; de Aldana, J.R.V.; Tan, Y.; Chen, F. Hybrid waveguiding structure in $LiTaO_3$ crystal fabricated by direct femtosecond laser writing. *Opt. Mater.* **2016**, *51*, 190–193. [CrossRef]

26. Nicolas, S.; Descroix, E.; Guyot, Y.; Joubert, M.F.; Abdulsabirov, R.Y.; Korableva, S.; Naumov, A.; Semashko, V. 4f2 to 4f5d excited state absorption in Pr3+-doped crystals. *Opt. Mater.* **2001**, *16*, 233–242. [CrossRef]
27. Gao, L.; Yang, X.; Shu, Y.; Chen, X.; Wang, J. Ionic liquid-based slab optical waveguide sensor for the detection of ammonia in human breath. *J. Colloid Interface Sci.* **2018**, *512*, 819–825. [CrossRef]